Nanoscale

PAPER

View Article Online
View Journal | View Issue

Cite this: *Nanoscale*, 2023, **15**, 5786

Influence of surface and intermolecular interactions on the properties of supported polyoxometalates†

Oliva M. Primera-Pedrozo, [a] Shuai Tan, [a] Difan Zhang, [a] Brian T. O'Callahan, [b] Wenjin Cao, [a] Eric T. Baxter,[a] Xue-Bin Wang, [a] Patrick Z. El-Khoury, [a] Venkateshkumar Prabhakaran, [a] Vassiliki-Alexandra Glezakou [c] and Grant E. Johnson *[a]

Polyoxometalates (POMs) with localized radical or open-shell metal sites have the potential to be used as transformative electronic spin based molecular qubits (MQs) for quantum computing (QC). For practical applications, MQs have to be immobilized in electronically or optically addressable arrays which introduces interactions with supports as well as neighboring POMs. Herein, we synthesized Keggin POMs with both tungsten (W) and vanadium (V) addenda atoms. Ion soft landing, a highly-controlled surface modification technique, was used to deliver mass-selected V-doped POMs to different self-assembled monolayer surfaces on gold (SAMs) without the solvent, counterions, and contaminants that normally accompany deposition from solution. Alkylthiol, perfluorinated, and carboxylic-acid terminated monolayers were employed as representative model supports on which different POM-surface and POM–POM interactions were characterized. We obtained insights into the vibrational properties of supported V-doped POMs and how they are perturbed by interactions with specific surface functional groups using infrared reflection absorption and scattering-type scanning near-field optical microscopy, as well as tip enhanced Raman spectroscopy. Different functional groups on SAMs and nanoscale heterogeneity are both shown to modulate the observed spectroscopic signatures. Spectral shifts are also found to be dependent on POM–POM interactions. The electronic structure of the V-doped POMs was determined in the gas phase using negative ion photoelectron spectroscopy and on surfaces with scanning Kelvin probe microscopy. The chemical functionality and charge transfer properties of the SAMs are demonstrated to exert an influence on the charge state and electronic configuration of supported V-doped POMs. The geometric and electronic structure of the POMs were also calculated using density functional theory. Our joint experimental and theoretical findings provide insight into how V substitution as well as POM-surface and POM–POM interactions influence the vibrational properties of POMs.

Received 2nd November 2022,
Accepted 22nd February 2023

DOI: 10.1039/d2nr06148a

rsc.li/nanoscale

Introduction

Several envisioned quantum computing (QC) architectures take full advantage of coherent electronic spins in open shell metal containing species and molecular radicals.[1] In practice, such spin centers have to be arranged into optically or electrically accessible quantum gates (QGs) capable of performing algorithmic operations.[2] Indeed, large scale QC will only be achieved if an appropriate and addressable set of QGs are arranged in a controlled and scalable manner.[3] Coordination complexes and magnetic molecules may be used to assemble two-qubit QGs that provide notable advantages over solid-state systems.[4] In particular, all molecules synthesized following a given chemical reaction are identical and their structures may be tailored extensively using established chemistry.[2] Coordination chemistry also provides a way of arranging multiple paramagnetic ions or assemblies of strongly coupled open shell metals within a molecule.[5] These species may be connected across multiple length scales through convenient and potentially switchable interactions.[6] Molecular metal

[a]*Pacific Northwest National Laboratory, Physical Sciences Division, P.O. Box 999, MSIN J7-10, Richland, Washington 99352, USA. E-mail: grant.johnson@pnnl.gov*
[b]*Pacific Northwest National Laboratory, Earth and Biological Sciences Division, P.O. Box 999, MSIN K8-88, Richland, Washington 99352, USA*
[c]*Oak Ridge National Laboratory, 1 Bethel Valley Road, Oak Ridge, Tennessee 37830, USA*

†Electronic supplementary information (ESI) available: Experimental and theoretical methods. Spectrum and table comparison of the *m*/*z* agreement between the experimentally measured and theoretically calculated isotope values for $VPOM^{4-}$ (PDF). See DOI: https://doi.org/10.1039/d2nr06148a

oxides, known as polyoxometalates (POMs), have additional advantages for QC such as being robust species that maintain their structural integrity in solution, in the solid state, and potentially in 2-dimensional (2D) arrays.[7] POMs may host single magnetic ions or groups of ions at defined sites in their rigid structure, leading to large magnetic molecules and clusters with defined topologies and symmetry.[2] Due to their multielectron reduction–oxidation (redox) activity, POMs may also accommodate different numbers of electrons while maintaining their geometric structure, making them valuable model systems with which to study the interplay between electron delocalization and magnetic exchange in high nuclearity clusters.[7–9]

Despite their advantages, increasing the spin coherence times of MQs supported in arrays remains a challenge that is hindering their use in QC.[3] Ensembles of identical weakly interacting spin centers are favored in this regard because there is a fine line between optimum coherent signal generation and onset of decoherence from spin centers interacting with one another and their environment.[10] Knowledge gaps remain regarding how the geometric and electronic structures of POMs and supports may be tailored to minimize different decoherence mechanisms (*i.e.*, nuclear spin diffusion, electron spin coupling, methyl rotation, spin–lattice relaxation, and spin diffusion barriers) and design qubit arrays with sufficiently long coherence times ($T > 100$ μs) for practical QC applications.[11] In particular, spins in supported molecules relax through spin–lattice interactions, making the surface-qubit interface an influential parameter determining the performance of MQ arrays.[12] Innovative approaches are needed to prepare and characterize well-defined arrays of supported MQs to achieve transformational advances in the understanding of spin decoherence mechanisms. Synthetic methods currently used to prepare magnetically doped POMs in solution usually result in a broad and poorly-defined distribution of products. The undefined composition of doped MQs, combined with the presence of solvent and counterions, often results in uncontrolled formation of aggregates and crystallites following drop casting onto surfaces from solution. Collectively, these confounding factors make it challenging to establish the structure–property relationships needed to inform the predictive design of MQ arrays with extended coherence times.

Ion soft landing (ISL) is a versatile technique that facilitates the preparation and modification of homogeneous films of mass-selected polyatomic ions in predetermined charge states through controlled deposition of gas-phase ions onto surfaces.[13–21] This distinguishing capability allows supported ions to be investigated in the absence of interference from counterions, solvent molecules, and other impurities that are present at interfaces prepared using solution based deposition.[22,23] In addition, soft landed ions are deposited without aggregation and crystallite formation.[24,25] Correspondingly, ISL is able to prepare the highest achievable coverage of discrete polyatomic ions and clusters dispersed homogeneously on surfaces. In particular, ISL has recently demonstrated itself to be a powerful technique for the controlled fabrication of well-defined POM-based interfaces for energy storage applications.[8,24–28]

Retention of charge by polyatomic ions soft landed onto self-assembled monolayers (SAMs) on gold was initially observed by Cooks and co-workers.[29] In subsequent investigations of inherently charged cations, we found that the 3+ charge state of Au_{11}^{3+} clusters was retained on fluorinated monolayers (FSAMs) up to a threshold surface coverage, while SAMs terminated with carboxyl (COOH–SAM) and methyl groups (HSAM) stabilized soft landed Au_{11}^{3+} clusters predominantly in the 2+ and 1+ charge states, respectively.[30,31] On HSAMs, cationic clusters underwent rapid charge reduction and neutralization through electron transfer from the underlying gold surface, while on FSAMs cationic clusters exhibited much slower charge reduction.[30] Retention of positive charge by soft landed cations on FSAMs is attributed to an energy barrier for electron transfer resulting from the electronegativity of the fluorine atoms in the SAM which induce a dipole at the Au–S interface.[32] In comparison, the charge retention and neutralization of negatively charged anions soft landed onto SAMs is remarkably different to that of cations. Specifically, triply charged POM anions were previously found to retain charge on all three SAM surfaces.[26,27] The unexpected charge retention was attributed to the large electron binding energies of the POM anions.[33]

POMs are known to undergo rapid and reversible multielectron redox processes while maintaining their geometric structure,[34] making them promising systems for a wide range of applications including electrochemical energy storage,[34] photochromic films,[35] and microelectronics.[36] In the context of MQs for potential QC, we focus herein on vanadium-doped tungsten Keggin POMs $[PV_xW_{12-x}O_{40}]^{(3+x)-}$ because they are amenable to solution synthesis with different numbers of V atoms, each of which introduces a spin-unpaired electron to the cluster. Alkylthiol (HSAM), hydrophobic perfluorinated alkylthiol (FSAM), and hydrophilic carboxylic acid (COOH–SAM) terminated monolayers on gold were selected as well-defined representative model supports on which to characterize POM-surface and POM–POM interactions relevant to potential QC applications.

In this paper, we report the electronic structure of $PVW_{11}O_{40}^{4-}$ ($VPOM^{4-}$), which was synthesized in solution and measured in isolation in the gas phase using electrospray ionization mass spectrometry (ESI-MS) and negative ion photoelectron spectroscopy (NIPES). The electronic properties of VPOMs soft landed on different SAMs was revealed using scanning Kelvin probe microscopy (KPFM). We investigated the vibrational properties of supported VPOMs and how they are influenced by interactions with different SAM surfaces using infrared reflection absorption spectroscopy (IRRAS) and nanoindentation enhanced tip enhanced Raman spectroscopy (TERS). The effect of POM surface coverage, and thereby POM–POM interactions on the vibrational modes of VPOMs, was also characterized using scattering-type scanning near-field optical microscopy (s-SNOM). The electronic structure and vibrational spectra of the POMs were modeled using density

functional theory (DFT) calculations. Our joint experimental and theoretical investigation offers insight into how intramolecular interactions between the substituted V atom and other atoms (W and O), as well as POM-surface and POM–POM intermolecular interactions influence the electronic and vibrational properties of supported POMs.

Results and discussion

The experimental and theoretical results are separated into two sections. The first section describes the electronic properties of $VPOM^{4-}$ in the gas phase and supported on different SAMs. The second section presents the vibrational properties of SAM-supported $VPOM^{4-}$.

Electronic properties of $VPOM^{4-}$ in the gas phase and supported on SAMs

Electrospray ionization mass spectrometry (ESI-MS). $VPOM^{4-}$ anions were prepared through a direct one step solution-phase synthesis and characterized using ESI-MS. Mass spectrometer conditions were optimized to minimize fragmentation of POMs through in-source collision induced dissociation so that mass spectra were representative of the species in solution.[37] As shown in Fig. 1a, the solution prepared by mixing $Na_3PO_4{\cdot}12WO_3{\cdot}xH_2O : NaVO_3$ salts in a molar ratio of 11 : 1 produced several V-doped POM anions with $VPOM^{4-}$ exhibiting the highest relative abundance in the mass spectrum. The mass spectrum of $WPOM^{3-}$ is provided in Fig. 1b for comparison. Notably, the ESI mass spectrum in Fig. 1a includes both the quadruply ($VPOM^{4-}$) and triply charged $[H^+][VPOM]^{4-}$ anions with the latter species resulting from association of a proton $[H^+]$ from water onto $VPOM^{4-}$ which helps to Coulombically stabilize the highly-charged 4- anion. To be confident of the molecular formula assignments, we obtained high mass resolution spectra for each of the anions observed in Fig. 1a. We compared the m/z accuracy and relative abundance of each of the experimentally measured isotopes in the overall isotopic envelopes of each POM anion against those calculated using the freely available mMass software (https://www.mmass.org/). Comparisons of the m/z accuracy of the experimentally measured isotopes with the corresponding theoretically calculated values for $VPOM^{4-}$ are presented in Fig. S1 and Table S1 of the ESI.† The results confirm the accurate formula assignment of $VPOM^{4-}$ (685.79 m/z) which matches the corresponding calculated theoretical m/z values with an error $\Delta m/z$ of −0.003.

Negative ion photoelectron spectroscopy (NIPES). To investigate how doping with a V atom influences the electronic structure and stability of $WPOM^{3-}$, the gas-phase photoelectron spectra of $VPOM^{4-}$ were recorded at photodetachment wavelengths of 193 and 157 nm, as shown in Fig. 2. More than eight spectral bands were resolved at 157 nm, with the first band having the lowest electron binding energy (EBE) labeled as X. Bands appearing at higher EBEs are notated alphabetically from A to G in ascending order (Fig. 2b). Notably, both the X and A bands of $VPOM^{4-}$ are in the negative EBE range. The X, A, and B bands are better resolved in the 193 nm spectrum in Fig. 2a, whereas the D band is substantially reduced in intensity and the E, F, and G bands are nearly completely suppressed. Suppression and disappearance of higher EBE bands at longer photodetachment wavelengths, even though their EBEs are appreciably smaller than the photon energy, is a hall-

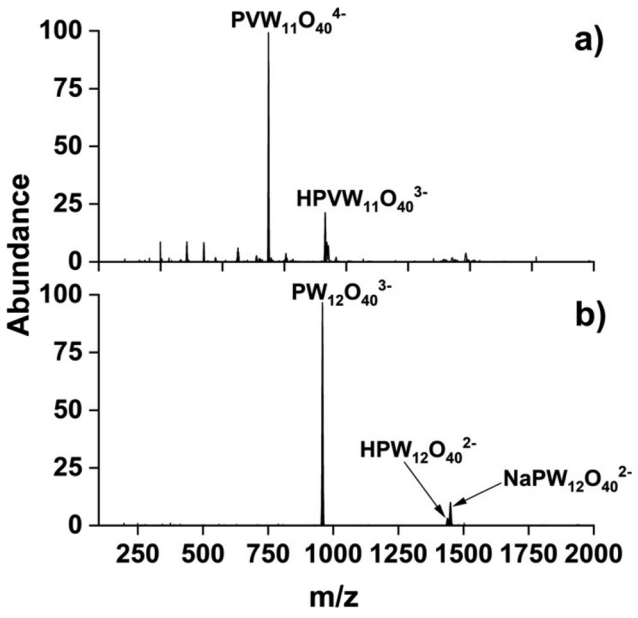

Fig. 1 Representative negative mode electrospray ionization mass spectra of (a) 100 μM $VPOM^{4-}$ solution in water prepared using an 11 : 1 molar ratio of $Na_3PO_4{\cdot}12WO_3{\cdot}xH_2O : NaVO_3$ salts, and (b) 100 μM $WPOM^{3-}$ solution in methanol prepared using $Na_3[PW_{12}O_{40}]{\cdot}xH_2O$.

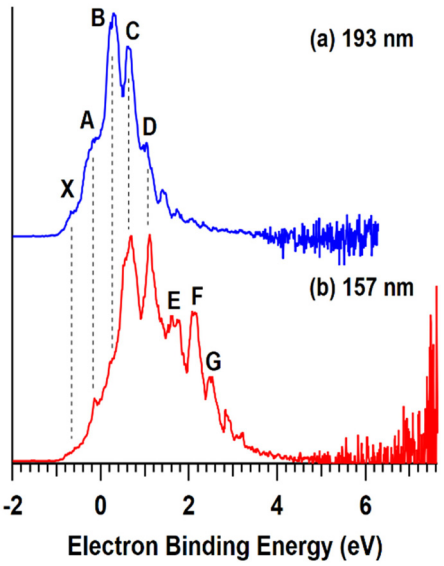

Fig. 2 T = 20 K negative ion photoelectron spectra of $VPOM^{4-}$ obtained at photodetachment wavelengths of (a) 193 and (b) 157 nm.

mark of photodetachment from multiply charged anions.[38] This characteristic behavior is due to the existence of repulsive Coulomb barriers (RCBs) against electron detachment that prevent electrons with kinetic energies smaller than the RCB from being emitted.[39–41] From the energy of the spectral band cutoff (*i.e.*, band D of 1.0 eV at 193 nm and band G of 2.4 eV at 157 nm) the magnitude of the RCB for $VPOM^{4-}$ is estimated to be 5.4 eV (photon energy minus the cutoff band EBE). This value indicates that a roughly 5.4 eV intramolecular coulombic repulsion exists in the quadruply-charged $VPOM^{4-}$ anion, which is about 2.0 eV higher than that for $WPOM^{3-}$ and $MoPOM^{3-}$. Previous work reported that these anions have the same RCB because of their similar size and identical ionic charge.[33] The adiabatic and vertical detachment energies (ADE, VDE) were measured from the threshold and maximum of the band X to be −0.9 and −0.63 eV, respectively, revealing that $VPOM^{4-}$ is an electronically unstable species in the gas phase, possessing 0.9 eV of excess energy against electron loss, but with a finite lifetime bestowed by the RCB. These electron detachment energies are substantially lower than those previously reported for pure $WPOM^{3-}$ (ADE = 2.1 and VDE = 2.3 eV) and indicate that POM-support and POM–POM interactions will play a critical role in stabilizing arrays of $VPOM^{4-}$ on different surfaces.

Theoretically calculated electron detachment energies. Density functional theory (DFT) calculations were performed to provide molecular-level insight into the geometric and electronic structures of $WPOM^{3-}$ and $VPOM^{4-}$. These calculations revealed ADE and VDE values for $WPOM^{3-}$ [ADE = 1.9 eV (exp. = 2.1 eV) and VDE = 2.2 eV (exp. = 2.3 eV)] and $VPOM^{4-}$ [ADE = −1.1 (exp. = −0.9 eV) and VDE = −0.7 eV (exp. = −0.6 eV)] that are in good agreement with the experimental NIPES measurements presented in Fig. 2. Electrostatic potential (ESP) maps were also calculated for these clusters and are provided in Fig. 3(a). As expected, $VPOM^{4-}$ has more negative charge at its surface compared to $WPOM^{3-}$. In addition, replacement of W with a V atom results in localization of electron density near the V atom, as indicated by the larger red areas in the lower right of Fig. 3a. The highest occupied and lowest unoccupied molecular orbitals (HOMO/LUMO) of $WPOM^{3-}$ and $VPOM^{4-}$ are also presented in Fig. 3b. Although the HOMO of both clusters is localized at bridging oxygen atoms, the LUMO of $WPOM^{3-}$ is delocalized over multiple W sites while the LUMO of $VPOM^{4-}$ is located predominately at the substituted V atom.

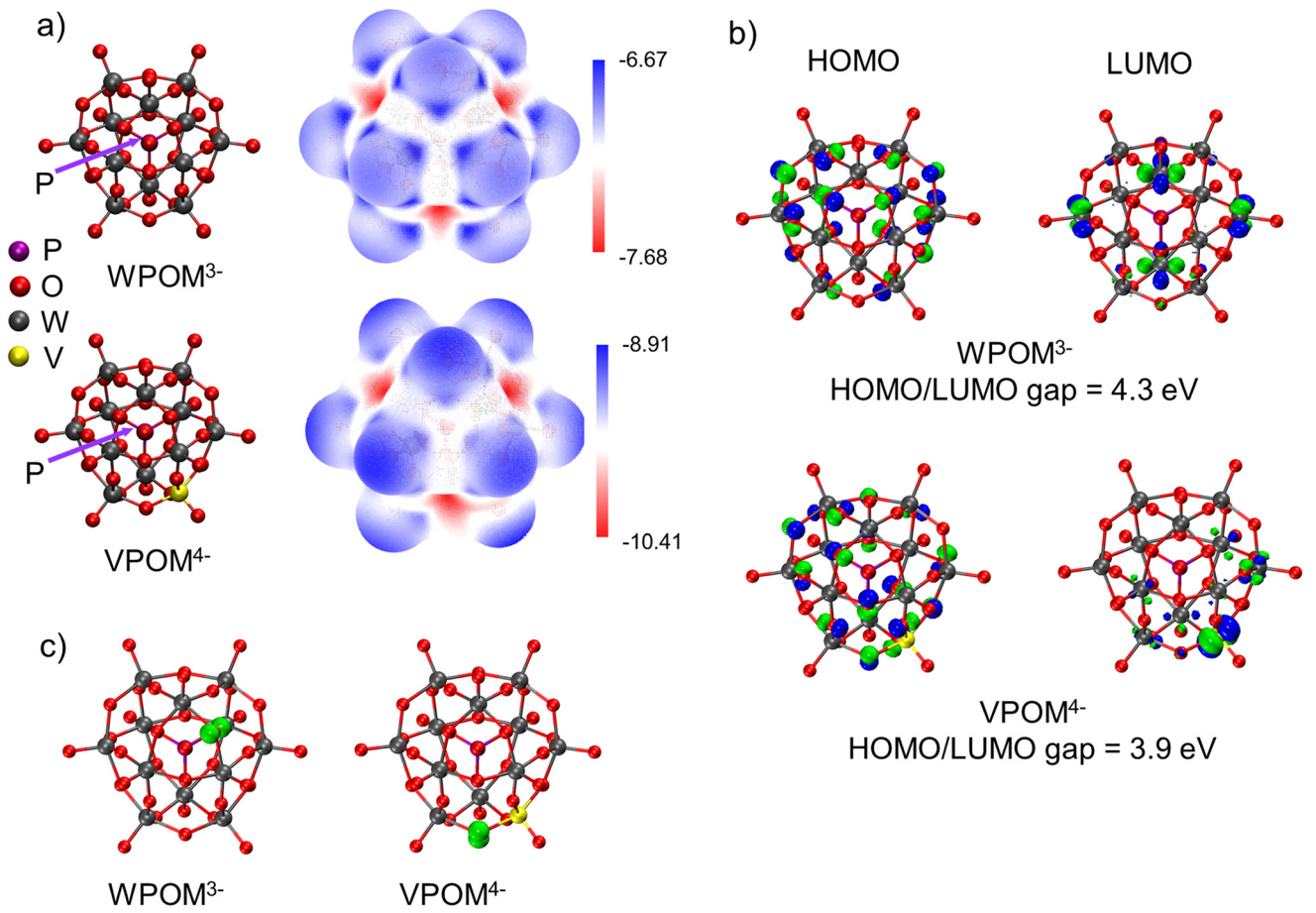

Fig. 3 (a) Calculated structures and electrostatic potential maps of $WPOM^{3-}$ and $VPOM^{4-}$ (P atom is located behind central O atom), (b) the highest occupied/lowest unoccupied molecular orbitals (HOMO/LUMO) of $WPOM^{3-}$ and $VPOM^{4-}$. Atoms follow the color scheme in (a), (c) calculated electron spin density of $WPOM^{3-}$ and $VPOM^{4-}$, highlighted in green. Atoms follow the color scheme in (a).

As a result, the HOMO/LUMO gap decreases from 4.3 eV for $WPOM^{3-}$ to 3.9 eV for $VPOM^{4-}$, suggesting that $VPOM^{4-}$ is less stable toward chemical reaction than $WPOM^{3-}$. The reduced HOMO/LUMO gap of $VPOM^{4-}$ has implications for the long-term stability of supported $VPOM^{4-}$ arrays. We also calculated the electron spin density when an electron is detached from both $WPOM^{3-}$ and $VPOM^{4-}$, as partial charge reduction of these ions is possible when they are supported on surfaces. The spin density, presented in Fig. 3(c), is localized on a bridging oxygen in $WPOM^{3-}$ and on the bridging oxygen atom nearest the V atom in $VPOM^{4-}$. Comparing the NIPE spectra of the quadruply charged $VPOM^{4-}$ anions presented in Fig. 2 with those of triply charged $MoPOM^{3-}$ and $WPOM^{3-}$ anions reported in a previous study,[33] the results show that replacing one group 6 metal atom (*i.e.*, Mo or W in a nominal +6 oxidation state) with V (*i.e.*, group 5, formally +5 oxidation state) releases one additional electron that amounts to a total charge of 4- for $VPOM^{4-}$. Therefore, doping $WPOM^{3-}$ with one V atom results in greatly reduced EBEs, from ADE = 1.7 eV in $MoPOM^{3-}$ and 2.1 eV in $WPOM^{3-}$ to −0.9 eV in $VPOM^{4-}$. The reduced EBE is largely driven by the increased intramolecular repulsion from 3.4 to 5.4 eV, gauged from the respective RCBs. Other factors that contribute to the low ADE = −0.9 eV for $VPOM^{4-}$ are chemical in nature. Specifically, earlier 3d transition metals tend to produce lower EBE species than their later 4d/5d counterparts in similar chemical structures and oxidation states.[33,42] Combined, V-doping makes the excess electron in $VPOM^{4-}$ thermodynamically more prone to transfer. This electron is located on a m2-oxo bridging oxygen, as indicated by the frontier occupied molecular orbitals (MOs). These results reveal important changes in the electronic structure of WPOM resulting from substitution of W with V that will play a critical role in determining the stability of supported $VPOM^{4-}$ arrays.

Scanning Kelvin probe force microscopy (KPFM) of supported $VPOM^{4-}$. After confirming the synthesis of $VPOM^{4-}$ and investigating its geometric and electronic structure in the gas phase, ISL was used to deposit a predetermined quantity of $WPOM^{3-}$ or $VPOM^{4-}$ onto three differently terminated SAM surfaces (*i.e.*, HSAM, COOH-SAM, and FSAM) on gold. ISL is a highly controlled surface modification technique which avoids complications that often confound the characterization and modeling of samples prepared using solution deposition (*e.g.*, aggregation, solvent, counterions). In the ISL experiments, ~1×10^{14} mass-selected $WPOM^{3-}$ or $VPOM^{4-}$ anions were delivered to the SAM surfaces in vacuum (~10^{-7} Torr) forming circular deposited regions ~3 mm in diameter. To investigate the electronic properties and charge retention of $VPOM^{4-}$ soft landed on different SAMs, the substrates were characterized *ex situ* both before and after ISL using an atomic force microscope (AFM) operated in the scanning Kelvin probe force microscopy (KPFM) mode. Previous experiments have demonstrated that changing the terminal chemical functionality of SAMs on Au modulates the work function (WF) of the substrate.[43] For example, the electronegative sulfur atoms of *n*-alkylthiol HSAMs generate a partially negatively charged region at the Au–S interface.[44] Together with simultaneous production of a corresponding partially positively charged CH_3-vacuum interface, the resulting charge polarization constitutes a macroscopic interface dipole that reduces the WF of the HSAM surface. This reduction in WF occurs because the electron emitted from the underlying Au surface is transported through the HSAM away from the partially negatively charged Au–S interface toward the partially positively charged methyl groups at the vacuum interface. In contrast, replacing the terminal methyl (CH_3) with more electronegative carboxyl (COOH-SAM) or fluorinated CF_3 (FSAM) groups generates a partially negatively charged SAM-vacuum interface.[44,45] Combined with simultaneous production of a corresponding partially positively charged Au–S interface, the resulting inverted interface dipole impedes electron transfer from the underlying gold surface through the SAM. Consequently, the WF increases in instances where electronegative -COOH or -CF_3 terminal groups are present at the vacuum interface. The three different SAMs investigated in this study were selected as model systems to explore how different chemical functionality and electron transfer properties of surfaces influence the electronic structure and vibrational modes of supported POMs.

As shown in Fig. 4a, the measured WFs of the bare SAMs increase in the order HSAM (5.03 eV) < COOH-SAM (5.09 eV) < FSAM (5.52 eV) (Table 1), revealing a trend that is consistent with previous studies.[44,46] Due to charge reduction and ion neutralization processes that occur between supported ions and SAM substrates, soft landed species may become partially neutralized following deposition.[13,14] Previous studies from our group demonstrated an approach combining experimental IRRAS measurements with DFT calculations to determine the distribution of anionic charge states of POMs supported on different SAMs. This method relies on correlations between the wavenumbers and shifts of characteristic vibrational modes [terminal metal–oxygen band (M=O_t), bridging metal–oxygen bands (M–$O_{b1,2}$–M)] and the ionic charge state of supported POMs. In our previous study, $WPOM^{3-}$ was found to partially retain its 3- charge on FSAMs while partially oxidized $WPOM^{2-}$ was observed to be the most abundant species on HSAMs. In general, the charge retention of soft landed anions on SAMs follows the order $q_{HSAM} < q_{COOH\text{-}SAM} < q_{FSAM}$. Herein, we used the measured WFs to better understand the ionic charge states and electronic structure of supported POMs. As shown in Fig. 4b, following soft landing of $WPOM^{3-}$ the WFs of all three SAMs were reduced and found to increase in the order HSAM (4.77 eV) < COOH-SAM (4.84 eV) < FSAM (4.94 eV). The global reduction in the WFs following deposition of $WPOM^{3-}$ on all three SAMs results from accumulation of negative charge at the SAM interface. In this case, electrons are emitted from the $WPOM^{3-}$ anions at the SAM interface where increased negative Coulombic repulsion is present, rather than from the underlying Au surface. As shown in Fig. 4c, the measured WFs of soft landed $VPOM^{4-}$ were found to be closer to those of the bare SAMs than $WPOM^{3-}$. Interestingly, the WF was observed to be larger (5.36 eV) on the HSAM than on the COOH-SAM (5.17 eV) or FSAM (5.11 eV). This finding contrasts

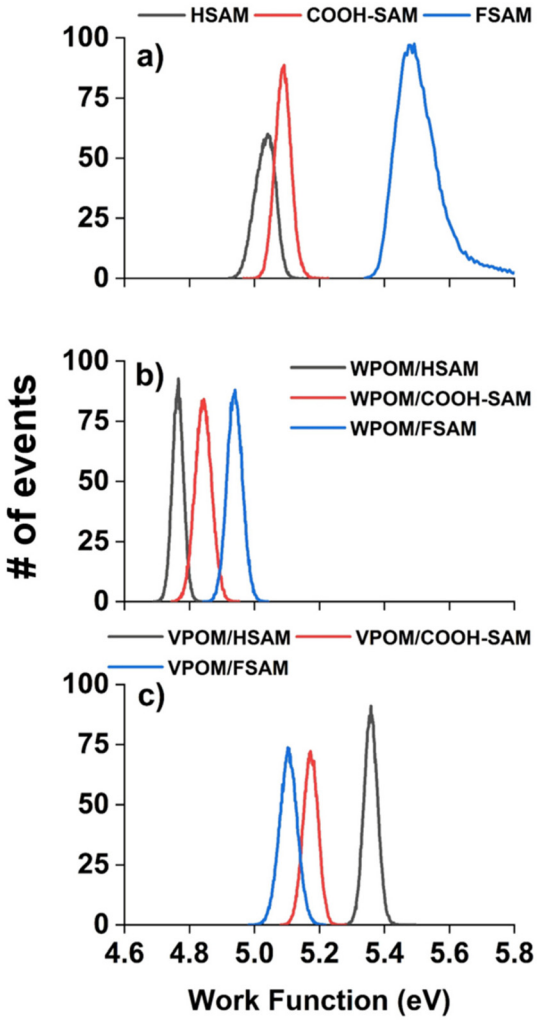

Fig. 4 Distribution of work function values measured over a 4 μm^2 area of (a) bare HSAM, COOH-SAM, and FSAM, (b) 1 × 10^{14} WPOM^{3-} soft landed on HSAM, COOH-SAM, and FSAM, and (c) 1 × 10^{14} VPOM^{4-} soft landed on HSAM, COOH-SAM, and FSAM.

with the results for the bare SAMs and SAMs with soft landed WPOM^{3-} where the relative WF increased in the order HSAM < COOH-SAM < FSAM. For VPOM^{4-}, the largest negative charge is expected to accumulate on the FSAM, resulting in increased Coulombic repulsion that reduces the WF (assuming electron emission from VPOM^{4-} rather than the Au surface). This repulsion builds up during deposition because ISL delivers only anions to the surface without any solvent or counter cations. In comparison, less negative charge from VPOM^{4-} is expected to be retained on the HSAM, resulting in less Coulombic repulsion and a higher WF. Similar to the results for WPOM^{3-}, in this case electrons are emitted from VPOM^{4-} anions at the vacuum interface rather than from the underlying Au surface. Based on the gas phase NIPES results presented in Fig. 2, the ADE and VDE of WPOM^{3-} are much higher than those of VPOM^{4-}, due to increased Coulombic repulsion in quadruply charged VPOM^{4-} compared to triply charged WPOM^{3-}. In comparison, the consistently larger WFs measured for VPOM^{4-} compared to WPOM^{3-} on all three SAMs suggests that the surface plays an important role in stabilizing POMs toward electron detachment, possibly through an image potential interaction with the underlying polarizable gold surface.[47] It is also possible that the larger charge accumulation resulting from soft landing of VPOM^{4-} compared to WPOM^{3-} was sufficient to promote spontaneous electron dissociation or transfer to the underlying gold surface.[31] In either case, this would result in formation of partially oxidized VPOM$^{3-,2-,1-}$ species with reduced overall negative charge and Coulombic repulsion and, therefore, increased WFs (assuming electron emission from VPOM^{4-}). These findings illustrate how substitution of a W atom with V influences the electronic structure and stability of VPOM^{4-} supported on surfaces with different chemical functionality and electron transfer properties. Finding the right balance of substitution and surface functionality will be critical to preserving the electronic and vibrational properties of POMs for potential use in MQ arrays.

Vibrational properties of supported VPOM^{4-}

Infrared reflection absorption spectroscopy (IRRAS) and theoretical calculations. To investigate how surface interactions influence the vibrational properties of supported POMs, we obtained IRRAS spectra of WPOM^{3-} or VPOM^{4-} soft landed on three different SAMs. The major vibrational features of POM^{3-} on SAMs have been characterized in detail previously.[26,27] To the best of our knowledge, the vibrational spectra of isolated VPOM^{4-} supported on well-defined surfaces has not been reported thus far.[48] For WPOM^{3-}, the main features reported in the literature for the asymmetric P–O stretch are found in the range of 1060–1080 cm^{-1} while the terminal W=O$_t$ stretch appears between 950–970 cm^{-1}.[26,27,49–51] Two different types of bridging tungsten–oxygen bands also contribute vibrational features observed at ~860–880 cm^{-1} (W–O$_{b2}$–W) and ~805–820 cm^{-1} (W–O$_{b1}$–W), respectively. Oxygen sites are identified as O$_i$ (internal), O$_t$ (terminal), Ob$_1$, (bridging 1), and Ob$_2$ (bridging 2). All of these characteristic IR bands of POMs have been reported previously in the literature

Table 1 Experimentally measured work functions of the bare SAM substrates on Au before and following soft landing of ~1 × 10^{14} WPOM^{3-} or VPOM^{4-} anions

Material	Work function (eV)	Material	Work function (eV)	Material	Work function (eV)
Bare HSAM	5.03	WPOM^{3-}/HSAM	4.77	VPOM^{4-}/HSAM	5.36
Bare COOH-SAM	5.09	WPOM^{3-}/COOH-SAM	4.84	VPOM^{4-}/COOH-SAM	5.17
Bare FSAM	5.52	WPOM^{3-}/FSAM	4.94	VPOM^{4-}/FSAM	5.11

and are observed in the IRRAS spectra of $WPOM^{3-}$ or $VPOM^{4-}$ presented in Fig. 5a. The presence of these peaks confirms the intact deposition of $WPOM^{3-}$ and $VPOM^{4-}$ onto the SAM surfaces. Additional deposition experiments performed at higher kinetic energies which induce fragmentation of POMs did not reveal these characteristic peaks.

To better understand and interpret the experimental IR features presented in Fig. 5a and the implications of their shifts on different SAMs, we used DFT calculations to determine the gas phase IR spectra of isolated $WPOM^{3-}$ and $VPOM^{4-}$. Snapshots of the structures used in these calculations are illustrated in Fig. 5b, and the theoretically predicted IR/Raman vibrational spectra are presented in Fig. 5c and d, respectively. In addition to the IR modes reported previously, the simulated vibrational spectra validate the peak assignments in the experimental spectrum (Fig. 5a). Specifically, $WPOM^{3-}$ exhibits two $W–O_{b1,2}–W$ peaks, one $W{=}O_t$ peak, and one $P–O_i$ peak in the range of 800–1200 cm^{-1}. Furthermore, the simulations identify additional peaks in the vibrational spectra of $VPOM^{4-}$ resulting from substitution of one W atom with V (1093–1107 cm^{-1}). For example, an additional peak is found at ~950 cm^{-1} in Fig. 5c which is not attributed to a single bond, but rather a combination band with contributions from both the $P–O_i$ and $W–O_b–W$ stretching vibrations. The $W{=}O_t$ mode in $VPOM^{4-}$ is comprised of two equally intense peaks located close to each other instead of the single peak observed for $WPOM^{3-}$. This difference in the IR spectra is consistent with the loss of molecular symmetry resulting from substitution of V for a W atom. In addition, the $P–O_i$ peak of $VPOM^{4-}$ is shifted to lower wavenumber compared to $WPOM^{3-}$ and a new V–O peak is also observed at ~1100 cm^{-1}. Another weak peak associated with $W{=}O_t$ is observed at higher wavenumber ~1150 cm^{-1} for $VPOM^{4-}$ that is not present in $WPOM^{3-}$. Previous reports in the literature used variations in this spectral feature to investigate vibrational signatures of V-substituted POMs.[52,53] Our results agree with this previous work on mono-substituted α-$(TBA)_4[PVW_{11}O_{40}]$ where two vibrational bands were found to be present. However, V_2POM^{5-} substituted with two V

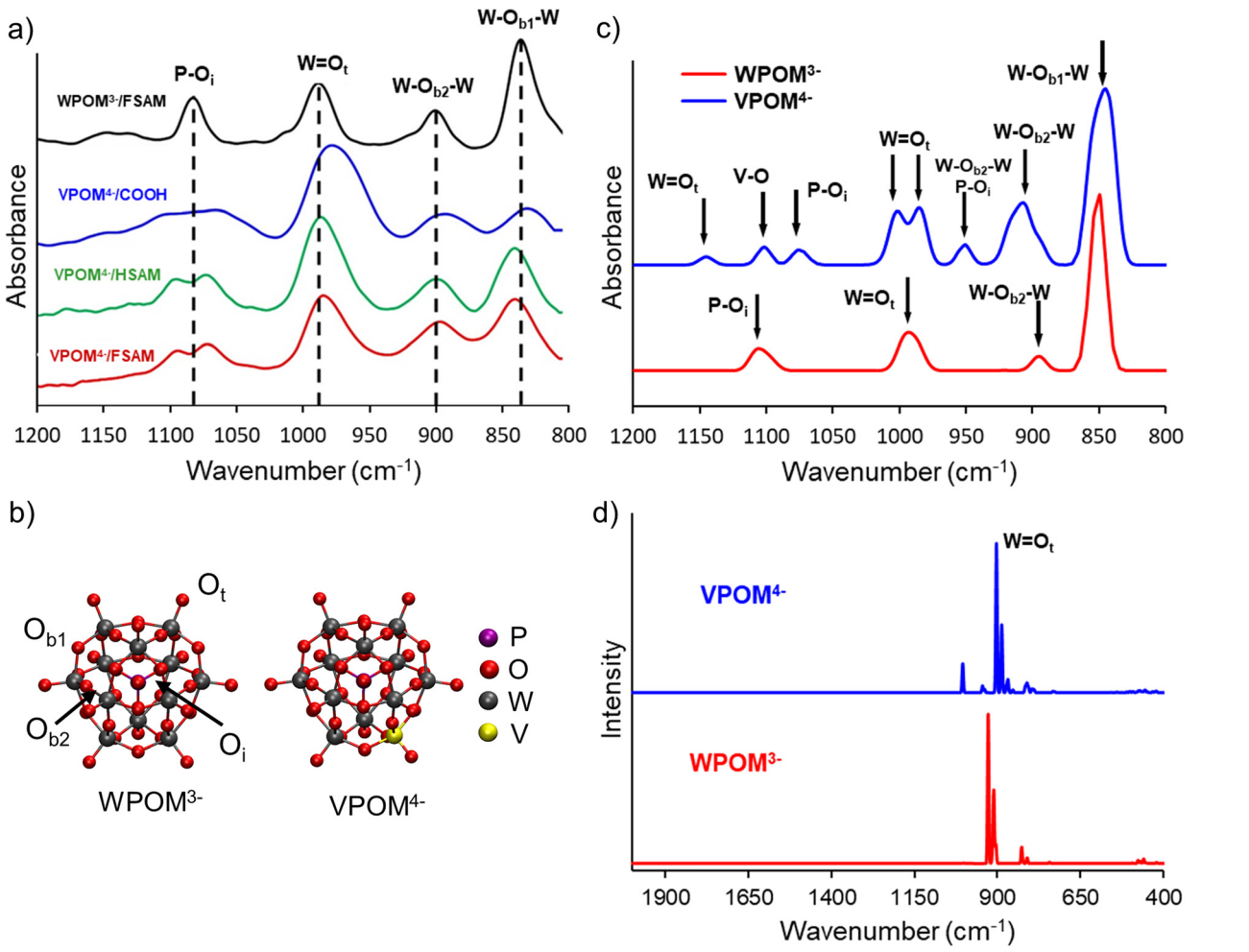

Fig. 5 (a) Experimental infrared reflection absorption spectroscopy spectra obtained following deposition of ~1 × 10^{14} $VPOM^{4-}$ ions on HSAM, COOH-SAM, and FSAM surfaces on Au. $WPOM^{3-}$ on FSAM is also shown for comparison, (b) theoretically calculated ground state structures of $WPOM^{3-}$ and $VPOM^{4-}$, four types of oxygen sites are identified as O_i (internal), O_t (terminal), Ob_1, and Ob_2 (bridging), (c) theoretically calculated IR spectra of gas phase $WPOM^{3-}$ and $VPOM^{4-}$, (d) theoretically calculated Raman spectrum of gas phase $VPOM^{4-}$ and $WPOM^{3-}$.

atoms, showed triplet combinations of vibrational bands for P–O_i, V=O_t, and W=O_t.

Comparison of the different IR spectra presented in Fig. 5 and Table 2 provides insight into how V substitution for W and interaction of POMs with the different terminal functional groups of SAMs influence their vibrational properties. For instance, the P–O mode, which appears as a single peak at 1084 cm^{-1} for $WPOM^{3-}$ on FSAM, is observed as two peaks spread across a broader wavenumber range for $VPOM^{4-}$ on all three SAMs. This difference is consistent with the reduction in molecular symmetry that accompanies the substitution of W with a V atom in the external metal–oxygen cage of $VPOM^{4-}$. In addition, the W=O_t peak, which appears at 988 cm^{-1} for $WPOM^{3-}$ on FSAM, is shifted to lower wavenumber for $VPOM^{4-}$ on all three SAMs. This shift is most pronounced for $VPOM^{4-}$ on the COOH-SAM surface where the peak appears at 978 cm^{-1}. A substantial shift in the W=O_t mode is reasonable considering that these bonds are located on the outside of the POM and, therefore, interact intimately with the SAM surface and adjacent POMs. Compared to $WPOM^{3-}$, shifts to lower wavenumber are also observed for the W–O_{b2}–W band of $VPOM^{4-}$ where the effect is again most prominent on the COOH-SAM. Compared to $WPOM^{3-}$, the W–O_{b1}–W bands of $VPOM^{4-}$ exhibit shifts to lower wavenumber on COOH-SAM and higher wavenumber on HSAM and FSAM. This difference may be attributed to the polar anionic character of carboxylate (COO^-) groups that may form through partial deprotonation of COOH. In comparison, the terminal CH_3 and CF_3 groups of the HSAM and FSAM are both nonpolar and comparatively inert.

In a previous study, we calculated how the different vibrational modes of $WPOM^{3-}$ shift as a function of the charge state of the supported POM.[27] Shifts in vibrational frequencies are also related to the interaction of Mo or W with the rest of the Keggin structure. For example, the IR peak positions of $WPOM^{3-}$ anions soft-landed on an FSAM surface shifted toward higher wavenumber when compared with other soft-landed anions such as $MoPOM^{3-}$. This finding may be related to the weaker bonding in $MoPOM^{3-}$ compared to $WPOM^{3-}$. The W=O_t band, in particular, exhibited a pronounced shift to higher wavenumber as the charge state of WPOM decreased from 3- to 2- to 1- to 0 due to oxidation. The W–$O_{b1,2}$–W bands also exhibited modest shifts to higher wavenumber with decreasing anionic charge of the WPOM. However, as shown in Fig. 5 and Table 2, most of the shifts observed for $VPOM^{4-}$ on the three SAMs were in the opposite direction toward lower wavenumber. Based on these findings, it appears that only a small amount of charge reduction or neutralization of $VPOM^{4-}$ occurs on the SAMs following soft landing, which is beneficial for maintaining the native electronic configuration of $VPOM^{4-}$.

Scattering-type scanning near-field optical microscopy (s-SNOM). To explore the spatial heterogeneity of the supported POMs, spatially-resolved IR s-SNOM spectra were acquired at regular positions across the ~3 mm diameter circular area of soft landed $VPOM^{4-}$ on all three SAMs. The resulting spatio-spectral datasets are presented in Fig. 6a–c where each line color indicates an IR spectrum obtained at a different position sequentially across the sample starting at the edge and moving in a straight line toward the center of the deposition. The ISL deposition technique has a unique advantage because the flux of the ion beam is most intense at the center and weakest near the edges. This inherent radial beam profile results in samples with a Gaussian-like distribution of surface coverages going from highest at the center of the deposition to lowest at the edges. Correspondingly, the IR absorbance is largest at the center of the spot where the POM coverage is highest and decreases towards the edge of the spot following a Gaussian-like trend. Interestingly, the wavenumber position of the W=O_t band (~988 cm^{-1}) is found to shift depending on the position (and surface coverage) as well as the type of SAM. For example, on the FSAM, the peak shifted from ~980 cm^{-1} at the edge of the deposited spot to ~987 cm^{-1} at the center. On the HSAM, we observed similar but less pronounced behavior where the W=O_t peak shifted from 978 cm^{-1} to 981 cm^{-1} across the deposited spot. In contrast, on the COOH-SAM a consistent peak position at 974 cm^{-1} was observed that did not change with the position or coverage of $VPOM^{4-}$. The shift of the W=O_t band to higher wavenumber near the center of the FSAM and HSAM may be explained by an increase in the surface coverage of $VPOM^{4-}$. Specifically, near the edges of the spot where the surface coverage is low, the soft landed $VPOM^{4-}$ interact primarily with the SAM surfaces because there is a large space between neighboring POMs. However, as the surface coverage increases near the center of the spot, the deposited POMs interact more with each other and less with the underlying support. Indeed, at

Table 2 Experimentally measured vibrational modes of ~1×10^{14} $WPOM^{3-}$ or $VPOM^{4-}$ anions soft landed onto HSAM, COOH-SAM, and FSAM surfaces on Au. The wavenumber shift compared to $WPOM^{3-}$ on FSAM is shown in parentheses. DFT calculated vibrational modes are provided for comparison

IR assignment	$WPOM^{3-}$ (cm^{-1}) FSAM (exp.)	$VPOM^{4-}$ (cm^{-1}) FSAM (exp.)	HSAM (exp.)	COOH-SAM (exp.)	Gas-phase (calc.)
V=O_t		1093	1093	1095	1107
P–O_a	1084	1074 (10)	1071 (13)	1067 (17)	1097
W=O_t	988	988 (0)	987 (1)	978 (10)	974
W–O_{b2}–W	900	901 (−1)	899 (1)	892 (8)	887
W–O_{b1}–W	836	845 (−9)	842 (−6)	835 (1)	845

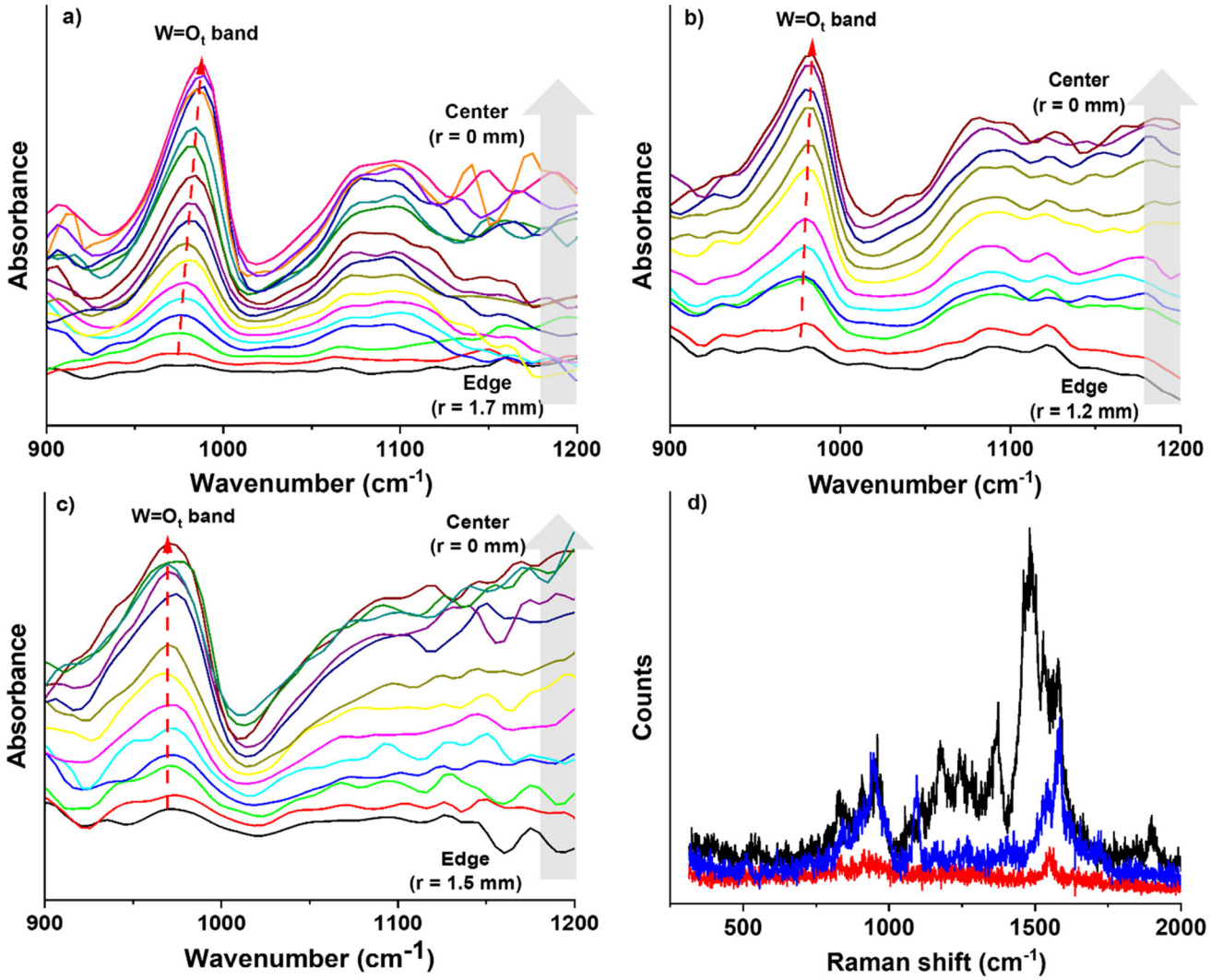

Fig. 6 Spatially-resolved infrared s-SNOM spectra obtained following deposition of 1 × 10^{14} $VPOM^{4-}$ ions on (a) FSAM, (b) HSAM, and (c) COOH-SAM surfaces on Au. The feature appearing at ~980 cm^{-1} corresponds to the terminal W═O_t vibrational band. Arrows from the bottom to the top indicate data collected from the edge (r = 1.2–1.7 mm) of the soft-landed sample to the center (r = 0 mm), (d) TERS spectra of $VPOM^{4-}$ obtained at three different positions in the same nanoindentation on FSAM/Au. The peaks observed beyond 1150 cm^{-1} may result from inter-cluster vibrations and the underlying SAM on Au.

sufficiently high coverage multiple layers of POMs may form that are not in direct contact with the SAM but rather with previously deposited POMs. Interestingly, POMs supported on the COOH-SAM do not exhibit the same shift in wavenumber as those deposited on HSAM and FSAM. The W═O_t band is also much broader on the COOH-SAM compared to the HSAM and FSAM, where this band appears sharper. The lack of a shift on the COOH-SAM may result from the presence of a fraction of deprotonated carboxylate anions (COO^-) on the surface that give the COOH-SAM a partial negative charge. A mixture of COOH and COO^- surface sites would also explain the broader W═O_t peak observed on the COOH-SAM. In comparison, no negative charge is present on the bare HSAM and FSAM so the change in charge at the surface following soft landing of $VPOM^{4-}$ may be more substantial than on the COOH-SAM. These results show that in addition to POM-surface interactions, POM–POM interactions play an important role in determining the vibrational properties of supported POMs.

Tip enhanced Raman spectroscopy (TERS). Further insights into the heterogeneity of potential MQ arrays were obtained from $VPOM^{4-}$ soft landed on FSAM using spatially resolved nanoindentation enhanced tip enhanced Raman spectroscopy (TERS). Conventional TERS measurements were attempted first but the signal-to-noise ratio for $VPOM^{4-}$ on SAMs was not sufficient to allow collection of reproducible Raman spectra. To overcome this challenge, we took advantage of imprinted plasmonic nanostructures prepared using pulsed-force nanolithography to enhance the TERS signal. Previous work demonstrated a 50× increase (on average) in TERS signal levels com-

pared to TERS acquired from a flat region of a gold substrate.[54] The Raman spectra obtained using this approach are presented in Fig. 6d where each line color indicates a spectrum acquired at a different location within a single nanoindentation. The peaks occurring in the range of 900–1000 cm^{-1} are consistent with the W=O_t vibrational modes reported previously in the literature for $WPOM^{3-}$.[55,56] The simulated Raman vibrational spectra from DFT calculations also reproduces such W=O_t peaks between 900–1000 cm^{-1}, as illustrated in Fig. 5d. Furthermore, unlike the experimental Raman spectra, the DFT simulated spectra do not show any peaks beyond 1150 cm^{-1}. Since the simulated Raman results correspond to the vibrations of POM clusters in the gas phase, the additional peaks observed in the experiments beyond 1150 cm^{-1} may result from inter-cluster vibrations and the underlying SAM on Au. The varying intensity of the three Raman spectra indicate different levels of enhancement depending on the position in a single nanoindentation. Differences in the relative intensity of the peaks between spectra suggest that even when using a highly-controlled deposition technique such as ISL, there is still substantial heterogeneity between different regions of supported POMs. These differences may result from varying orientations of the reduced symmetry $VPOM^{4-}$ on the surface as well as from disordered regions of the SAMs. These findings emphasize the importance of spatially-resolved spectroscopic probes in understanding the role of nanoscale heterogeneity in determining the properties of materials for potential QC applications.

Conclusions

POMs have the potential to be used as transformative electronic spin-based MQs for QC applications. In practical devices, MQs have to be immobilized in addressable arrays to form QGs that are capable of performing algorithmic operations. The array environment introduces unavoidable interactions of MQs with supports as well as with neighboring POMs. Therefore, understanding POM-surface and POM–POM interactions and how they may be harnessed to maximize spin coherence times is central to developing addressable MQ arrays. In this contribution, ISL was used to deposit mass-selected $VPOM^{4-}$ onto three different SAM surfaces on gold which were used as representative model systems on which to characterize support and intermolecular interactions. ISL avoids the complications inherent to deposition from solution and provides well-defined samples that are amenable to detailed spectroscopic characterization and high-level theoretical modeling. The electronic structure of $VPOM^{4-}$ synthesized in solution was determined in the gas phase using NIPES and on three different SAMs using scanning KPFM. The terminal chemical functionality and charge transfer properties of the SAMs were shown to exert an influence on the charge state and electronic configuration of supported $VPOM^{4-}$. The vibrational modes of $VPOM^{4-}$ and their perturbation through interactions with surfaces were also explored using IRRAS and TERS revealing that different functional groups on SAMs and nanoscale heterogeneity both modulate the observed spectroscopic signatures. The effect of surface coverage and intermolecular interactions on the vibrational properties of $VPOM^{4-}$ was also investigated using spatially-resolved s-SNOM revealing spectral shifts that are dependent on POM-support and POM–POM interactions. The geometric and electronic structure of the POMs, along with their vibrational spectra, were also calculated using DFT to provide molecular-level insight into the stability and local spin density in $VPOM^{4-}$. Collectively, our findings provide insight into how V substitution for W as well as different POM-surface and POM–POM interactions influence the electronic and vibrational properties of supported POMs. The vibrational properties of POMs modulate spin–lattice decoherence rates which determine the suitability of MQ arrays for potential QC applications.

Author contributions

The manuscript was written through contributions of all authors. All authors have given approval to the final version of the manuscript.

Conflicts of interest

There are no conflicts of interest to declare.

Acknowledgements

O. M. P., S. T., D. Z., B. T. O., and E. T. B acknowledge support from the Laboratory Directed Research and Development Program at PNNL. G. E. J., V. P., and V.-A. G. were partially supported by the U.S. Department of Energy (DOE), Office of Science, Office of Basic Energy Sciences, Chemical Sciences, Geosciences, and Biosciences Division, project 72353 (Interfacial Structure and Dynamics in Separations). P. Z. E., X.-B.W., and W. C. were partially supported by the U.S. Department of Energy (DOE), Office of Science, Office of Basic Energy Sciences, Division of Chemical Sciences, Geosciences, and Biosciences (Chemical Kinetics and Dynamics at Interfaces, FWP 16248). V. A. G. was partially supported by the laboratory directed research and development program (LDRD) at Oak Ridge National Laboratory. Part of this work was performed using EMSL, a National Scientific User Facility sponsored by the DOE's Office of Biological and Environmental Research and located at the Pacific Northwest National Laboratory (PNNL). PNNL is a multiprogram national laboratory operated by Battelle for the U.S. Department of Energy under contract DE-AC05-76RL01830. Computer resources were provided by Research Computing at PNNL and the National Energy Research Scientific Computing Center (NERSC), a DOE Office of Science User Facility operated under contract DE-AC02-05CH11231.

References

1 M. R. Wasielewski, *et al.*, Exploiting chemistry and molecular systems for quantum information science, *Nat. Rev. Chem.*, 2020, **4**, 490–504.
2 G. Aromi, D. Aguila, P. Gamez, F. Luis and O. Roubeau, Design of magnetic coordination complexes for quantum computing, *Chem. Soc. Rev.*, 2012, **41**, 537–546.
3 M. J. Graham, J. M. Zadrozny, M. S. Fataftah and D. E. Freedman, Forging Solid-State Qubit Design Principles in a Molecular Furnace, *Chem. Mater.*, 2017, **29**, 1885–1897.
4 J. Lehmann, A. Gaita-Arino, E. Coronado and D. Loss, Quantum computing with molecular spin systems, *J. Mater. Chem.*, 2009, **19**, 1672–1677.
5 A. Gaita-Arino, F. Luis, S. Hill and E. Coronado, Molecular spins for quantum computation, *Nat. Chem.*, 2019, **11**, 301–309.
6 R. E. P. Winpenny, Quantum Information Processing Using Molecular Nanomagnets As Qubits, *Angew. Chem., Int. Ed.*, 2008, **47**, 7992–7994.
7 J. M. Clemente-Juan, E. Coronado and A. Gaita-Arino, Magnetic polyoxometalates: from molecular magnetism to molecular spintronics and quantum computing, *Chem. Soc. Rev.*, 2012, **41**, 7464–7478.
8 V. Prabhakaran, G. E. Johnson, B. B. Wang and J. Laskin, In situ solid-state electrochemistry of mass-selected ions at well-defined electrode-electrolyte interfaces, *Proc. Natl. Acad. Sci. U. S. A.*, 2016, **113**, 13324–13329.
9 T. Ueda, Electrochemistry of Polyoxometalates: From Fundamental Aspects to Applications, *ChemElectroChem*, 2018, **5**, 823–838.
10 G. A. Timco, *et al.*, Engineering the coupling between molecular spin qubits by coordination chemistry, *Nat. Nanotechnol.*, 2009, **4**, 173–178.
11 C. J. Yu, *et al.*, Spin and Phonon Design in Modular Arrays of Molecular Qubits, *Chem. Mater.*, 2020, **32**, 10200–10206.
12 M. J. Amdur, *et al.*, Chemical control of spin-lattice relaxation to discover a room temperature molecular qubit, *Chem. Sci.*, 2022, **13**, 7034–7045.
13 J. Laskin, G. E. Johnson, J. Warneke and V. Prabhakaran, From Isolated Ions to Multilayer Functional Materials Using Ion Soft Landing, *Angew. Chem., Int. Ed.*, 2018, **57**, 16270–16284.
14 G. E. Johnson, D. Gunaratne and J. Laskin, Soft- and reactive landing of ions onto surfaces: Concepts and applications, *Mass Spectrom. Rev.*, 2016, **35**, 439–479.
15 J. Cyriac, T. Pradeep, H. Kang, R. Souda and R. G. Cooks, Low-Energy Ionic Collisions at Molecular Solids, *Chem. Rev.*, 2012, **112**, 5356–5411.
16 S. Rauschenbach, M. Ternes, L. Harnau and K. Kern, Mass Spectrometry as a Preparative Tool for the Surface Science of Large Molecules, *Annu. Rev. Anal. Chem.*, 2016, **9**, 473–498.
17 S. Rauschenbach, *et al.*, Electrospray ion beam deposition of clusters and biomolecules, *Small*, 2006, **2**, 540–547.
18 A. Tata, C. Salvitti and F. Pepi, From vacuum to atmospheric pressure: A review of ambient ion soft landing, *Int. J. Mass Spectrom.*, 2020, **450**, 116309.
19 A. Walz, K. Stoiber, A. Huettig, H. Schlichting and J. V. Barth, Navigate Flying Molecular Elephants Safely to the Ground: Mass- Selective Soft Landing up to the Mega-Dalton Range by Electrospray Controlled Ion-Beam Deposition, *Anal. Chem.*, 2022, **94**, 7767–7778.
20 S. Kahle, *et al.*, The Quantum Magnetism of Individual Manganese-12-Acetate Molecular Magnets Anchored at Surfaces, *Nano Lett.*, 2012, **12**, 518–521.
21 A. Saywell, *et al.*, Self-assembled aggregates formed by single-molecule magnets on a gold surface, *Nat. Commun.*, 2010, **1**, 4392.
22 G. E. Johnson, Q. C. Hu and J. Laskin, Soft Landing of Complex Molecules on Surfaces, *Annu. Rev. Anal. Chem.*, 2011, **4**, 83–104.
23 N. Vats, *et al.*, Electron microscopy of polyoxometalate ions on graphene by electrospray ion beam deposition, *Nanoscale*, 2018, **10**, 4952–4961.
24 V. Prabhakaran, *et al.*, Rational design of efficient electrode-electrolyte interfaces for solid-state energy storage using ion soft landing, *Nat. Commun.*, 2016, **7**, 11399.
25 G. E. Johnson, *et al.*, DRILL Interface Makes Ion Soft Landing Broadly Accessible for Energy Science and Applications, *Batteries Supercaps*, 2018, **1**, 97–101.
26 K. D. D. Gunaratne, *et al.*, Controlling the Charge State and Redox Properties of Supported Polyoxometalates via Soft Landing of Mass-Selected Ions, *J. Phys. Chem. C*, 2014, **118**, 27611–27622.
27 K. D. D. Gunaratne, V. Prabhakaran, A. Andersen, G. E. Johnson and J. Laskin, Charge retention of soft-landed phosphotungstate Keggin anions on self-assembled monolayers, *Phys. Chem. Chem. Phys.*, 2016, **18**, 9021–9028.
28 V. Prabhakaran, *et al.*, Controlling the Activity and Stability of Electrochemical Interfaces Using Atom-by-Atom Metal Substitution of Redox Species, *ACS Nano*, 2019, **13**, 458–466.
29 S. A. Miller, H. Luo, S. J. Pachuta and R. G. Cooks, Soft-landing of polyatomic ions at fluorinated self-assembled monolayer surfaces, *Science*, 1997, **275**, 1447–1450.
30 G. E. Johnson, T. Priest and J. Laskin, Charge Retention by Gold Clusters on Surfaces Prepared Using Soft Landing of Mass Selected Ions, *ACS Nano*, 2012, **6**, 573–582.
31 G. E. Johnson, T. Priest and J. Laskin, Coverage-Dependent Charge Reduction of Cationic Gold Clusters on Surfaces Prepared Using Soft Landing of Mass-Selected Ions, *J. Phys. Chem. C*, 2012, **116**, 24977–24986.
32 D. M. Alloway, *et al.*, Interface dipoles arising from self-assembled monolayers on gold: UV-photoemission studies of alkanethiols and partially fluorinated alkanethiols, *J. Phys. Chem. B*, 2003, **107**, 11690–11699.
33 T. Waters, *et al.*, Photoelectron Spectroscopy of free multiply charged keggin anions alpha-$[PM_{12}O_{40}]^{3-}$ (M = Mo, W) in the gas phase, *J. Phys. Chem. A*, 2006, **110**, 10737–10741.

34 H. Wang, *et al.*, In Operand X-ray Absorption Fine Structure Studies of Polyoxometalate Molecular Cluster Batteries: Polyoxometalates as Electron Sponges, *J. Am. Chem. Soc.*, 2012, **134**, 4918–4924.
35 S. Q. Liu, H. Mohwald, D. Volkmer and D. G. Kurth, Polyoxometalate-based electro- and photochromic dual-mode devices, *Langmuir*, 2006, **22**, 1949–1951.
36 D. Velessiotis, *et al.*, Molecular junctions made of tungsten-polyoxometalate self-assembled monolayers: Towards polyoxometalate-based molecular electronics devices, *Microelectron. Eng.*, 2011, **88**, 2775–2777.
37 M. T. Ma, *et al.*, Gas-Phase Fragmentation of Polyoxotungstate Anions, *Inorg. Chem.*, 2009, **48**, 598–606.
38 X.-B. Wang and L.-S. Wang, Photoelectron Spectroscopy of Multiply Charged Anions, *Annu. Rev. Phys. Chem.*, 2009, **60**, 105–126.
39 L.-S. Wang and X.-B. Wang, Probing Free Multiply Charged Anions Using Photodetachment Photoelectron Spectroscopy, *J. Phys. Chem. A*, 2000, **104**, 1978–1990.
40 X.-B. Wang and L.-S. Wang, Observation of negative electron-binding energy in a molecule, *Nature*, 1999, **400**, 245–248.
41 J. Warneke, *et al.*, Electronic Structure and Stability of $[B_{12}X_{12}]^{2-}$ (X = F–At): A Combined Photoelectron Spectroscopic and Theoretical Study, *J. Am. Chem. Soc.*, 2017, **139**, 14749–14756.
42 X. Yang, *et al.*, Photoelectron spectroscopy of free polyoxoanions $Mo_6O_{19}^{2-}$ and $W_6O_{19}^{2-}$ in the gas phase, *J. Phys. Chem. A*, 2004, **108**, 10089–10093.
43 F. Rissner, *et al.*, Understanding the Electronic Structure of Metal/SAM/Organic–Semiconductor Heterojunctions, *ACS Nano*, 2009, **3**, 3513–3520.
44 H. Fukushima, *et al.*, Microstructure, Wettability, and Thermal Stability of Semifluorinated Self-Assembled Monolayers (SAMs) on Gold, *J. Phys. Chem. B*, 2000, **104**, 7417–7423.
45 H. Wang, S. Chen, L. Li and S. Jiang, Improved Method for the Preparation of Carboxylic Acid and Amine Terminated Self-Assembled Monolayers of Alkanethiolates, *Langmuir*, 2005, **21**, 2633–2636.
46 H. Ron, S. Matlis and I. Rubinstein, Self-assembled monolayers on oxidized metals. 2. Gold surface oxidative pre-treatment, monolayer properties, and depression formation, *Langmuir*, 1998, **14**, 1116–1121.
47 N. D. Lang and W. Kohn, Theory of Metal-Surfaces - Induced Surface Charge and Image Potential, *Phys. Rev. B*, 1973, **7**, 3541–3550.
48 J. C. Orozco, D. T. Shuaib, C. L. Marshall and M. I. Khan, Divanadium substituted keggin $[PV_2W_{10}O_{40}]$ on non-reducible supports-Al_2O_3 and SiO_2: synthesis, characterization, and catalytic properties for oxidative dehydrogenation of propane, *React. Kinet., Mech. Catal.*, 2020, **131**, 753–768.
49 R. Thouvenot, M. Fournier, R. Franck and C. Rocchiccioliderltcheff, Vibrational Investigations of Polyoxometalates .3. Isomerism in Molybdenum(VI) and Tungsten(VI) Compounds Related to the Keggin Structure, *Inorg. Chem.*, 1984, **23**, 598–605.
50 P. Su, V. Prabhakaran, G. E. Johnson and J. Laskin, In Situ Infrared Spectroelectrochemistry for Understanding Structural Transformations of Precisely Defined Ions at Electrochemical Interfaces, *Anal. Chem.*, 2018, **90**, 10935–10942.
51 X. Lopez, J. M. Maestre, C. Bo and J. M. Poblet, Electronic properties of polyoxometalates: A DFT study of alpha/beta-$[XM_{12}O_{40}]^{n-}$ relative stability (M=W, Mo and X a main group element), *J. Am. Chem. Soc.*, 2001, **123**, 9571–9576.
52 M. J. Watras and A. V. Teplyakov, Infrared and computational investigation of vanadium-substituted Keggin $[PV_nW_{12-n}O_{40}]^{n+3-}$ polyoxometallic anions, *J. Phys. Chem. B*, 2005, **109**, 8928–8934.
53 O. Dmitrenko, *et al.*, Effect of cations in infrared and computational analysis of vanadium-containing six-coordinate oxotungstates, *J. Phys. Chem. B*, 2003, **107**, 7747–7752.
54 C. F. Wang, B. T. O'Callahan, A. Krayev and P. Z. El-Khoury, Nanoindentation-enhanced tip-enhanced Raman spectroscopy, *J. Chem. Phys.*, 2021, **154**, 241101.
55 C. Rocchiccioliderltcheff, M. Fournier, R. Franck and R. Thouvenot, Vibrational Investigations of Polyoxometalates .2. Evidence for Anion Anion Interactions in Molybdenum(VI) and Tungsten(VI) Compounds Related to the Keggin Structure, *Inorg. Chem.*, 1983, **22**, 207–216.
56 A. J. Bridgeman, Density functional study of the vibrational frequencies of alpha-Keggin heteropolyanions, *Chem. Phys.*, 2003, **287**, 55–69.